

Contents lists available at ScienceDirect

# Petroleum Science

journal homepage: www.keaipublishing.com/en/journals/petroleum-science



# Original Paper

# Quantitative characterizations of anisotropic dynamic properties in organic-rich shale with different kerogen content



Jian-Yong Xie <sup>a, b, \*</sup>, Yan-Ping Fang <sup>a, b</sup>, Xing-Hua Wu <sup>a, b</sup>, Jian'er Zhao <sup>a, b</sup>, Jun-Cheng Dai <sup>c</sup>, Jun-Xing Cao <sup>a</sup>, Ji-Xin Deng <sup>a</sup>

- <sup>a</sup> State Key Laboratory of Oil and Gas Reservoir Geology and Exploitation, Chengdu University of Technology, Chengdu, 610059, Sichuan, China
- b Key Lab of Earth Exploration & Information Techniques of Ministry of Education, Geophysical Institute, Chengdu University of Technology, Chengdu, 610059. Sichuan. China
- <sup>c</sup> PetroChina Southwest Oil & Gasfield Company, Chengdu, 610017, Sichuan, China

#### ARTICLE INFO

Article history:
Received 20 February 2023
Received in revised form
25 June 2023
Accepted 7 October 2023
Available online 11 October 2023

Edited by Jie Hao and Meng-Jiao Zhou

Keywords: Elastic properties Organic shale Anisotropy Kerogen content Physical modeling

#### ABSTRACT

Understanding the quantitative responses of anisotropic dynamic properties in organic-rich shale with different kerogen content (KC) is of great significance in hydrocarbon exploration and development. Conducting controlled experiments with a single variable is challenging for natural shales due to their high variations in components, diagenesis conditions, or pore fluid. We employed the hot-pressing technique to construct 11 well-controlled artificial shale with varying KC. These artificial shale samples were successive machined into prismatic shape for ultrasonic measurements along different directions. Observations revealed bedding perpendicular P-wave velocities are more sensitive to the increasing KC than bedding paralleling velocities due to the preferential alignments of kerogen. All elastic stiffnesses except  $C_{13}$  are generally decreasing with the increasing KC, the variation of  $C_{11}$  and  $C_{33}$  on kerogen content are more sensitive than those of C<sub>44</sub> and C<sub>66</sub>. Apparent dynamic mechanical parameters ( $\nu$  and E) were found to have linear correlation with the true ones from complete anisotropic equations independent of KC, which hold value towards the interpretation of well logs consistently across formations. Anisotropic mechanical parameters ( $\Delta E$  and brittleness  $\Delta B$ ) tend to decrease with the reducing KC, with  $\Delta B$  showing great sensitivity to KC variations. In the range of low KC (<10%), the  $V_P/V_S$  ratio demonstrated a linearly negative correlation with KC, and the V<sub>P</sub>/V<sub>S</sub> ratio magnitude of less than 1.75 may serve as a significant characterization for highly organic-rich (>10%) shale, compilation of data from natural organic rich-shales globally verified the similar systematic relationships that can be empirically used to predict the fraction of KC in shales.

© 2023 The Authors. Publishing services by Elsevier B.V. on behalf of KeAi Communications Co. Ltd. This is an open access article under the CC BY-NC-ND license (http://creativecommons.org/licenses/by-nc-nd/4.0/).

## 1. Introduction

Shale represents a vast energy resource for future gas production and has gained increasing significance (Montgomery et al., 2005; Sonnenberg and Pramudito, 2009). It typically displays pronounced inherent anisotropy, which holds great importance in seismic processing and the imaging of structures in crosshole tomography studies (Banik, 1984; Sayers, 2005). Achieving high-precision seismic processing, accurate interpretation, and reliable constraints for rock-physical models necessitate a comprehensive

understanding of anisotropy (Allan et al., 2015). However, there is currently insufficient knowledge regarding the influence of multiple sources on the anisotropic dynamic properties.

Organic-rich shales possess intrinsically complex structure with inorganic matrix and organic matter. Previous researches on shale anisotropy are mainly focus on preferred alignment of clay platelets (Kaarsberg, 1959; Jones and Wang, 1981; Wenk et al., 2007; Kanitpanyacharoen et al., 2011; Sayers and Boer, 2019; Ding et al., 2020a) and bedding paralleled micro-crack (Johnston and Christensen, 1995; Dewhurst and Siggins, 2006; Baird et al., 2017; Li et al., 2020). As an original component of forming the intricate matrix of shale rocks, organic matter is also regarded as a crucial variable that determining the intrinsic anisotropy (Tissot and Bernard, 1984; Prasad et al., 2011). Establishment of the

<sup>\*</sup> Corresponding author. E-mail address: xjyshl@sina.com (J.-Y. Xie).

quantitative relationship between the organic matter and anisotropic dynamic properties is not only pivotal to understand the induced mechanisms of anisotropy, but also to provide potential relationship for indication of kerogen content from seismic profile. Since kerogen content is a significant parameter in the evaluation of the organic abundance and production potential of shale reservoirs (Yu et al., 2017), it has considerable impact on the rock quality, shale gas-in-place estimations and organic-rich rocks assessment from surface seismic and well logs (Passey et al., 2010; Løseth et al., 2011). Many attempts were motivated to experimentally investigate such relations, Passey et al. (2010) proposed that kerogen content may have more impacts than expect on the elastic properties due to its low density based on the SEM observations. Vernik and Milovac (2011) indicated that  $V_P/V_S$  ratio may be an effective tool to distinguish the organic-rich shale according to the rock data analysis. Zhu et al. (2011) presented the increasing kerogen content in shale would enhance the anisotropy by analyzing the well logging data, while Sone and Zoback (2013) experimentally observed an opposite phenomenon. Alsinan (2017) discussed the relationship between the elastic properties and organic matter with Nanodetection technology. With raman spectrometer, Khatibi et al. (2017) studied the relationship between the mechanical/elastic properties and kerogen with different maturity. Zhao et al. (2018) presented that sum of porosity and kerogen content has a linear relationship with acoustic impedance based on statistical experi-

It should be noted that the majority of studies conducted on shale have focused on natural rock samples, which present significant limitations. These limitations include a low volume of available rock with variable kerogen content, limited quantity of samples, and strong heterogeneity, as well as chemical and mechanical instability in natural shale cores. Consequently, these studies have provided qualitative or semi-quantitative results, and in some cases, contradictory findings have emerged, as seen in the works of Zhu et al. (2013) and Sone and Zoback (2013). Furthermore, it is challenging to account for the dynamic property response triggered by specific factors in real shale samples (Bohacs et al., 2005).

Recently, many researchers tried to construct artificial shale models which were based on the cold-pressing technique (Luan et al., 2014, 2016; Altowairqi et al., 2015; Beloborodov et al., 2017; Ding et al., 2020b, 2021), and made many differences in dealing with brittleness, anisotropy and compaction. However, during the cold-pressing procedure, they did not take account diagenesis temperature which may bring uncertainty. Xie et al. (2019) proposed a novel hot-pressing technique to construct well-controlled artificial shale to investigate the relationship between the elastic properties and kerogen content, which made a great progress to promote the quantitatively controlled method, and concluded that the crossplot of  $\lambda \rho$  versus  $\mu \rho$  color coded by kerogen in various confining pressure may predict kerogen content. However, all the data are measured on cylinder samples that are cored in only one direction of paralleling to the bedding plane. As known, due to the anisotropic characterizations which aroused by the spatial distribution of organic matter, the dynamic properties could be changed with the directions. Shale is generally described as being a transversely isotropic (TI) medium with a symmetric axis, which becomes the most conventional approach to characterizing the anisotropy of shale (Xie et al., 2015, 2018). In this sense, description of anisotropic dynamic properties needs five stiffness constants which require wave speeds three strategic directions (0°, 45° and 90°) with respect to the symmetry axis. Consequently, the response of dynamic properties of shales with different kerogen content should further investigate by taking account of anisotropic features.

In this study, our main focus is to establish the quantitative

correlations between the kerogen content and directional dynamic properties, while considering anisotropy in organic-rich shale. To achieve this objective, we constructed 11 well-consolidated artificial shale (WCAS) samples using the hot-pressing technique. These samples were deliberately created with varying kerogen content ranging from approximately 1%-15%. The hot-pressing technique takes into account both the temperature and pressure conditions necessary for proper diagenesis (Xie et al., 2019). Following the construction of the WCAS samples, we shaped them into prismatic forms and employed pulse transmission techniques to measure the compressional and shear wave speeds in strategic directions relative to the bedding within the samples. These measurements were taken under ambient conditions. Based on these measurements, we established quantitative relationships between the weight percentage of kerogen content and various dynamic elastic properties such as velocities, stiffnesses, anisotropy, and the  $V_P/V_S$  ratio. Additionally, we also established relationships between the kerogen content and dynamic mechanical properties such as Young's modulus (E) and Poisson's ratio ( $\nu$ ) in different directions.

## 2. Sample description and similarity evaluations

## 2.1. Physical modeling and facilities

Organic-rich shale is compacted and consolidated of finegrained (typically less than 4 µm) non-organic minerals (clay, siliceous and carbonaceous) and organic debris under complicated diagenetic conditions (pressure, temperature and time). The data sets of original mineral components and their associated weight percentage for both organic matter and nonorganic compositions (Fig. 1) were measured from the cored natural shale from the main gas-bearing shale reservoir around the world. Consequently, the original components for the models are selected with powders of quartz, calcite, illite and organic matters. Fig. 2 shows the SEM observations of the original component that confirm the particles of non-organic matters are smaller than 4 µm. EDS detection are also performed to distinguish the minerals. The powder organic matters exhibit ball-shape with varied grain sizes (Fig. 2d), and obtaining sufficient quantities of natural kerogen from samples cannot practically yield enough material for the construction of analog samples. After substantial trail work, an acceptable

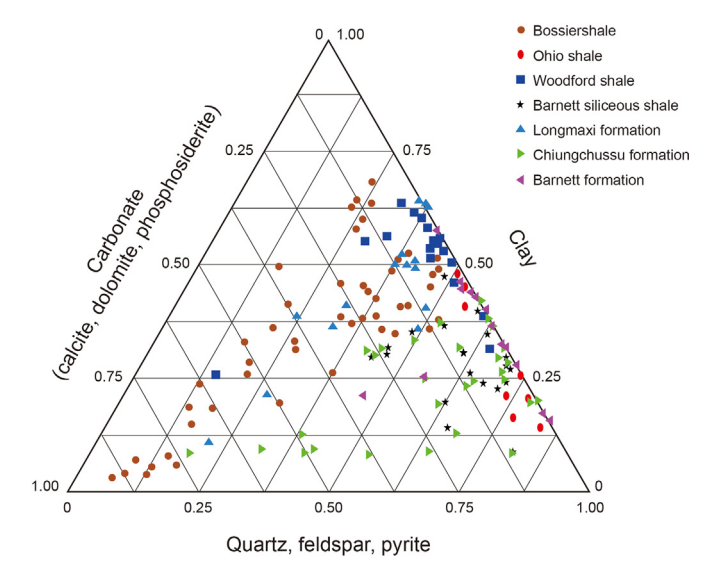


**Fig. 1.** Inorganic components and weight percentages of main shale reservoir around the world (Adapted from Bowker, 2002; Passey et al., 2010; Jiang et al., 2010).

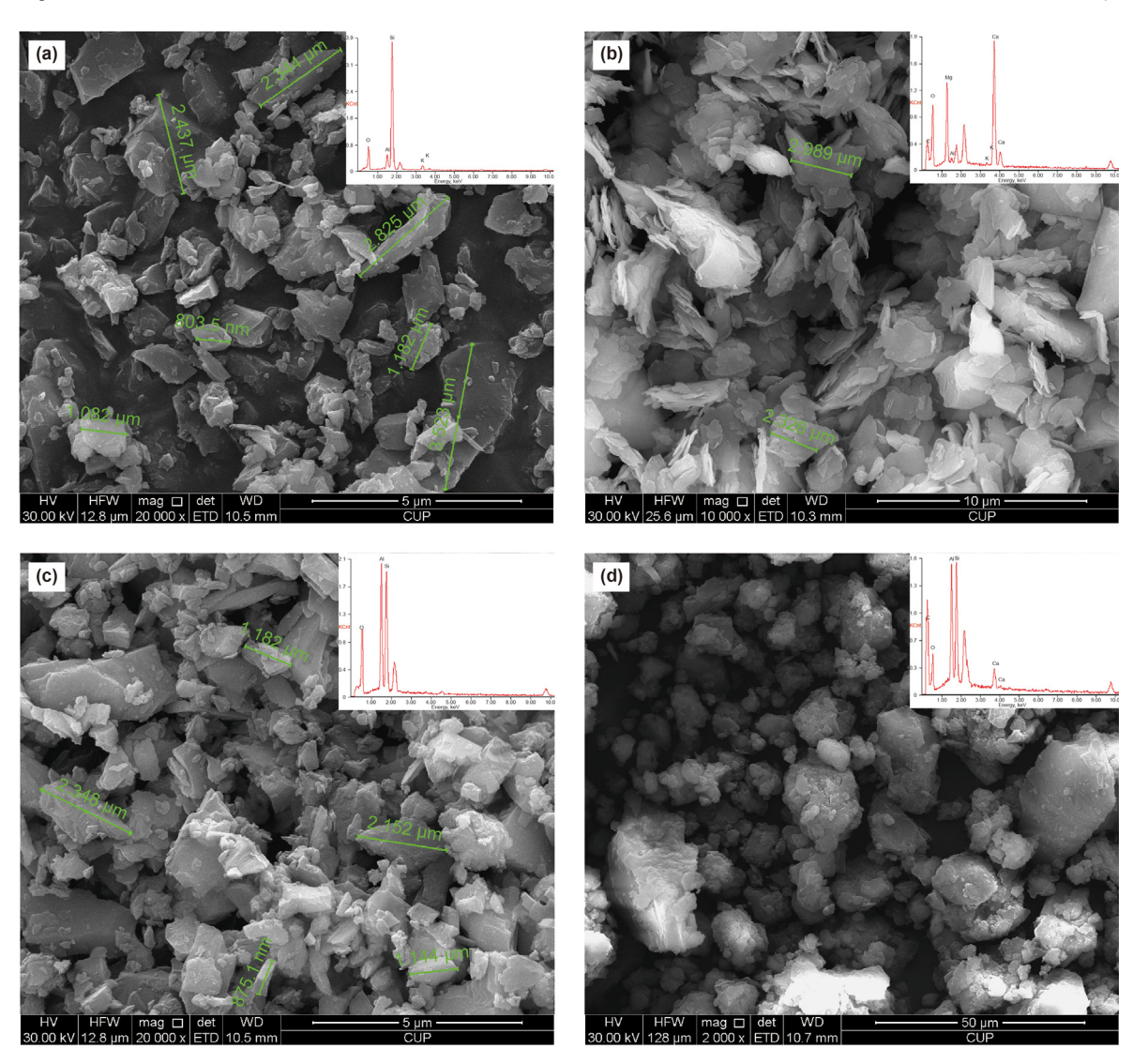


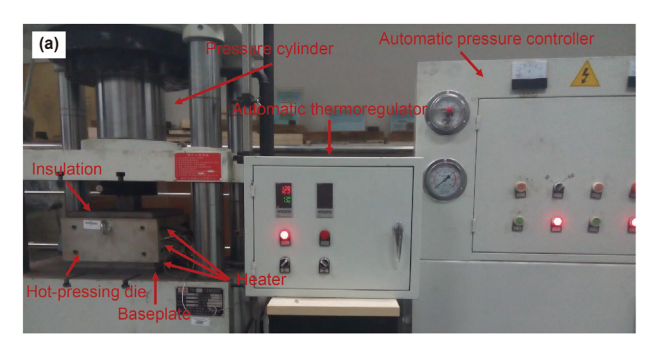
Fig. 2. SEM observations of the original compositions of WCAS samples. (a) Powdered quartz, (b) powdered illite (flaky structures), (c) powdered calcite and (d) powdered organic matters. The corresponding FDS results are also exhibited in the image

alternative called humic substance which is obtained from the repository of a fertilizer Ltd. in China satisfied the requirement. The similarity evaluation between the kerogen analog and natural kerogen can be found in our earlier work (Xie et al., 2016, 2019), and elastic properties of the analog are estimated with density of 1.5 g/cm<sup>3</sup>, bulk and shear modulus of 3.1 GPa and 3.0 GPa, respectively.

In order to simulate the diagenetic environment (temperature and pressure) of natural organic-rich shale and further consolidate the mixture of powdered components into solid sample, a hotpressing physical modeling system (HPPMS) was designed as shown in Fig. 3a (more details in Xie et al., 2019). Fig. 3b shows the schematic diagram of the hot-pressing mould. Six heaters are installed in the wearing layer uniformly which are used to provide and control the diagenetic temperature. An inconel-sheathed thermocouple pyrometer is installed adjacently to the cavity in the wearing layer, so that it can monitor the temperature in the die in real-time and send the acquired data to the controller. Variation of temperature within the die to be tested was probably less than 3 °C based on measurements. The temperature controller can set the predefined value of temperature, control the increasing or decreasing heat rate as well as compensate the heat while below

and cool the die while exceed the predefined value. The four-column hydraulic press system consists of energy conversion device (pump, oil cylinder), energy adjustion device (valve), energy transform device (oil tank, piping) and crate controller. With the controlling of electric system, the movable crossbeam can be driven automatically.

The procedure of hot-pressing procedure can be described straightforwardly as below: the hydraulic press system exerts the uniaxial stress of predefined value on the indenter of the die; the predefined stress and dwell time are set and displaying on the controller. Simultaneously, the electric heating pipe generates heat into cavity, which is filled with the mixed selected composition, thereby achieve the effect of hot-pressing. Construction of the artificial samples generally consists of 5 steps: (1) Ball mill the selective original mineral components powders into evenly solid powder mixtures (SPM), noting that the selected original components should be dried at 60 °C for 12 h at least in oven to avoid agglomeration during the mix procedure, and each component should be placed in different ovens separately. (2) Interfuse the SPM and adhesive into fully and evenly solid and liquid mixtures (SLM), (3) Stuff the SLM into the hot-pressing die. Other details (e.g.



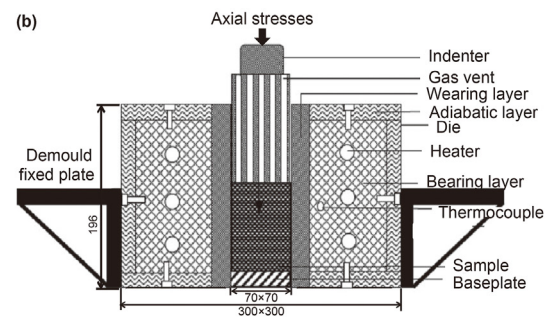


Fig. 3. (a) Picture of automatic hot-pressing die system (HPDS); (b) Schematic diagram of the hot pressing mould.

the set parameters of planetary ball mill, mesh of sieve) for the first three steps can be find in Luan et al. (2016). (4) Apply hot-pressing procedure. It can be divided into three steps: pre-compaction & heating-up, hot-pressing preservation and heat preservation. Based on our experience after substantial trial experiments, the parameters for step I of pre-compaction can be set as 1 MPa for 30 min, the time of hot-pressing preservation should be more than 4320 min, and the preset parameters of steps III for heat preservation can be 50 °C for 1440 min before removal from the hot-pressing die, and the aforementioned parameter in each step would significantly enhance the success rate of constructing a well-formed model. (5) Demold from the die.

## 2.2. Experimental evaluation

After being demoulded from the hot-pressed die, SEM detection of a freshly broken surface was done in WCAS sample (cored along and normal to the bedding plane) at high magnification. Fig. 4a and b show the SEM observations for the nonorganic mineral with layered texture in the different directions respectively, which exhibit high similarity to those of natural shale. Fig. 5a and b show two typical micro-distributions of flow-shape and globule-shape for our WCAS, which are also similar to the SEM observations on the typical microstructures (distinct globular shapes and more lenticular shapes) of kerogen in natural shale (Zargari et al., 2013), and the flowed-shape kerogen would be more likely exhibited preferred orientations along the bedding which may affect the anisotropy, and globule-shaped kerogen would be more likely enhance the homogeneity of the sample. We have also made attempts to observe the distribution of organic matter on larger scales. However, it is challenging to differentiate typical structures

at the centimeter scale. More details on the similarity evaluations between the WCAS and natural shale can be seen in Xie et al. (2019). With total-angle ultrasonic test system (Xie et al., 2015), both compressional and shear wave with interval of 10° were measured in a horizontal cored WCAS sample which exhibit strong anisotropy (Fig. 6), which further strengthen the necessity of directional investigation for dynamic properties for the shale.

## 3. Theoretical background

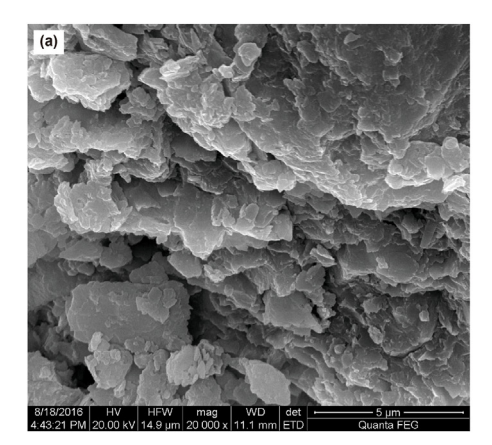
Shale samples can be regarded as VTI (vertical transversely isotropic) medium with the rotational symmetry axis, using Voigt's notation, Hook's Law relating stress  $\sigma$  to strain  $\epsilon$  may be expressed as

$$\sigma = \begin{bmatrix} \sigma_1 \\ \sigma_2 \\ \sigma_3 \\ \sigma_4 \\ \sigma_5 \\ \sigma_6 \end{bmatrix} = \begin{bmatrix} C_{11} & C_{11} - 2C_{66} & C_{13} & 0 & 0 & 0 \\ C_{11} - 2C_{66} & C_{11} & C_{13} & 0 & 0 & 0 \\ C_{13} & C_{13} & C_{33} & 0 & 0 & 0 \\ 0 & 0 & 0 & C_{44} & 0 & 0 \\ 0 & 0 & 0 & 0 & C_{44} & 0 \\ 0 & 0 & 0 & 0 & 0 & C_{66} \end{bmatrix} \begin{bmatrix} \epsilon_1 \\ \epsilon_2 \\ \epsilon_3 \\ 2\epsilon_4 \\ 2\epsilon_5 \\ 2\epsilon_6 \end{bmatrix} = C\epsilon,$$

$$(1)$$

where  $C_{11}$ ,  $C_{33}$ ,  $C_{44}$   $C_{66}$  and  $C_{13}$  are stiffnesses to describe the relationship between the stress and strain for a VTI medium. The five stiffnesses can be calculated by measuring elastic wave velocities (Mah and Schmitt, 2001; Sarout et al., 2007):

$$C_{11} = \rho V_{PX}^2,$$
 (2)



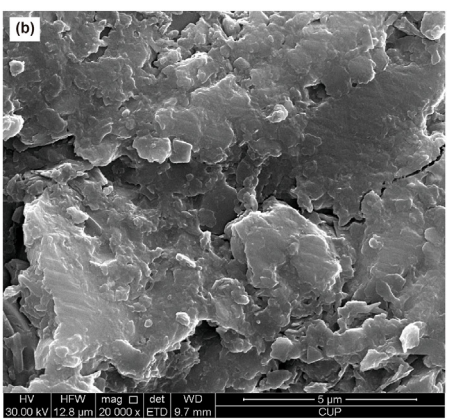
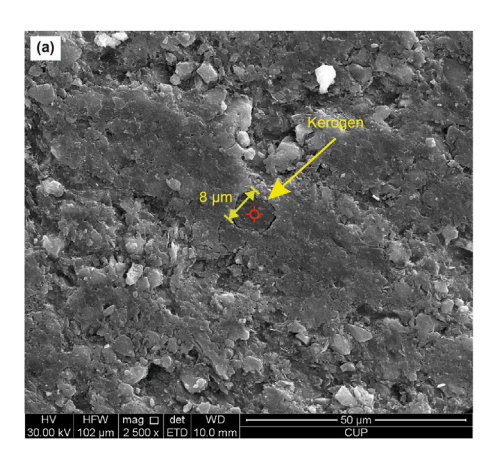


Fig. 4. SEM observations for micro-distribution of the aligned clay (a) along and (b) normal to the bedding in the WCAS.



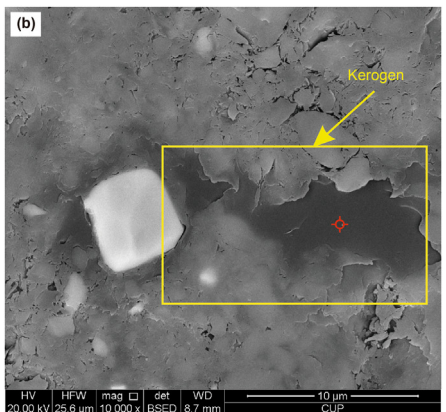
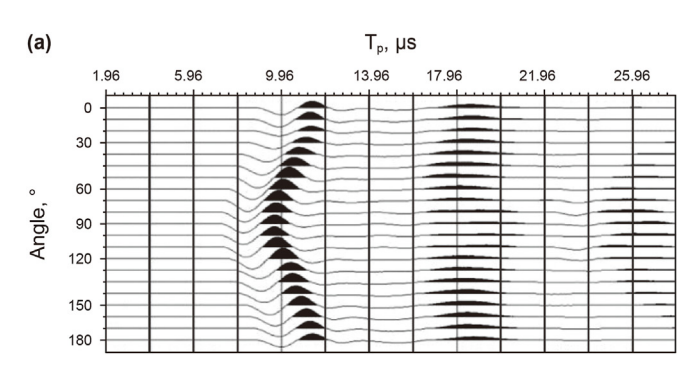
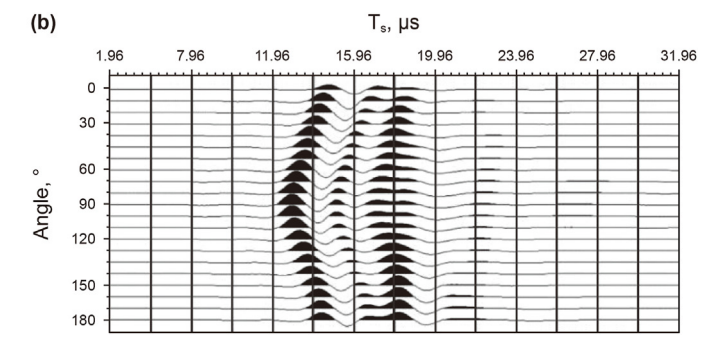


Fig. 5. Two typical shapes for the micro-distribution of kerogen in WCAS samples with SEM observations. (a) Ball shape, (b) "flow" shape.





**Fig. 6.** Waveforms of (a) compressional wave and (b) shear wave at 0° to 180° to the bedding plane with interval of 10°, both compressional and shear wave for the WCAS sample exhibit strong anisotropy.

$$C_{33} = \rho V_{PZ}^2,$$
 (3)

$$C_{44} = \rho V_{SVZ}^2, \tag{4}$$

$$C_{66} = \rho V_{\text{SHX}}^2, \tag{5}$$

$$C_{13} = -C_{44} + \frac{1}{2} \sqrt{\left(C_{11} + C_{33} + 2C_{44} - 4\rho V_{P_{450}}^2\right)^2 - \left(C_{11} - C_{33}\right)^2},$$
(6)

The P-wave  $\epsilon$  and S-wave  $\gamma$  anisotropic parameters are easily calculated using Thomsen (1986)

$$\varepsilon = \frac{C_{11} - C_{33}}{2C_{33}},\tag{7}$$

$$\gamma = \frac{C_{66} - C_{44}}{2C_{44}},\tag{8}$$

and

$$\delta = \frac{(C_{13} + C_{44})^2 - (C_{33} - C_{44})^2}{2C_{33}(C_{33} - C_{44})},\tag{9}$$

For a VTI medium, dynamic Young's moduli E and Poisson's ratio v can be experimentally determined by elastic constants (Mavko et al., 2009):

$$E_{11} = \frac{4C_{66} \left[ C_{33} (C_{11} - C_{66}) - C_{13}^2 \right]}{C_{11}C_{33} - C_{13}^2}$$
 (10)

$$E_{33} = \frac{C_{33}(C_{11} - C_{66}) - C_{13}^2}{C_{11} - C_{66}} \tag{11}$$

$$v_{12} = \frac{C_{12}C_{33} - C_{13}^2}{C_{11}C_{33} - C_{13}^2} \tag{12}$$

$$v_{31} = \frac{C_{13}}{C_{11} + C_{12}} \tag{13}$$

$$v_{13} = \frac{C_{13}(C_{11} - C_{12})}{C_{11}C_{33} - C_{13}^2} \tag{14}$$

where  $E_{11}$  and  $E_{33}$  are dynamic Young's modulus in the direction along and normal to the bedding.  $v_{ij}$  refers to ratio of transverse strain  $\varepsilon_i$  to axial strain  $\varepsilon_i$  with a uniaxial stress applied as  $\sigma_i$ .

To describe the anisotropic mechanical properties for the shale, we define the Young's modulus anisotropic parameter  $\Delta E$ , the Poisson's ratio anisotropic parameter  $\Delta \nu$  and Brittleness anisotropic parameter  $\Delta B$  as follows:

$$\Delta E = \frac{E_{11} - E_{33}}{E_{11}} \tag{15}$$

$$\Delta v = \frac{v_{13} - v_{12}}{v_{13}} \tag{16}$$

$$\Delta B = \frac{B_{11} - B_{33}}{B_{11}} \tag{17}$$

where  $B_{11}$  and  $B_{33}$  are calculated based on Rickman et al. (2008) as follows:

$$B_{11} = \frac{E_{11\_Nor} + v_{13\_Nor}}{2}, B_{33} = \frac{E_{33\_Nor} + v_{31\_Nor}}{2}$$
 (18)

$$E_{ij-Nor} = \frac{E_{ij} - E_{min}}{E_{max} - E_{min}}, \quad v_{ij-Nor} = \frac{v_{max} - v_{ij}}{v_{max} - v_{min}}$$
(19)

 $E_{ij\mathrm{-Nor}}$  and  $v_{ij\mathrm{-Nor}}$  denote the normalized Young's modulus and Poisson's ratio.

## 4. Experimental measurement and results

Based on the technique workflow (Xie et al., 2019), 11 cuboid WCAS samples (7 cm  $\times$  7 cm  $\times$  6.6 cm) which exhibit high similarity to the natural shale are constructed with different kerogen content (in the range from 1 to 15 wt%). Noted that each component of the inorganic matter for the samples are controlled by weight and remain unchanged (300 g quartz, 250 g illite, 25 g calcite), they are not saturated any fluid and exhibit black in color, and stratified structures are not distinct on the macroscopic view. The densities of samples are in the range of 2.1 and 2.28 g/cm<sup>3</sup>, which are measured by the Archimedean displacement method with variance of 0.5%. The porosities of the eleven samples range from 2.86% to 6.75% which is achieved with He expansion based on Boyle's law. Ultrasonic velocities of compressional (V<sub>P</sub>) and shear wave (both V<sub>SV</sub> and V<sub>SH</sub>) of all the 11 samples were firstly tested in the vertical and horizontal directions of loading with 0.5 MHz transducers at room pressure and temperature after being demouded from the die (Fig. 7a). Cuboid WCAS samples were then cut into a prismatic (multi-faced polyhedron) shape for the ultrasonic measurement at different angles to the bedding (Fig. 7b). The basic dataset of the WCAS samples can be seen in Table 1, noting that the measurement of velocities in the off-axis angle 45° to the bedding plane for WCAS samples #1, #2 and #11 are failed due to the fracture occurring in these samples during the trimmed process. Error determination of the ultrasonic pulse transmission technique are based on the study by Yin (1992) or Hornby (1998), which give relative errors of our measurement by 0.7% for the P-wave and 1.2% for S-wave velocity estimation.

It is important to assess the influence of kerogen content on wave speeds in different directions, both V<sub>P</sub> and V<sub>S</sub> were measured in the directions of X, Y, Z axis as well as at an off-axis angle 45° from the bedding plane as refer to Fig. 7b. Generally, both for V<sub>P</sub> and V<sub>S</sub> exhibit to decrease with the increasing kerogen content. The observations of wave speeds broadly indicate that these blocks have transverse isotropic symmetry, too. To briefly review, the wave speeds in the principal directions of a perfect TI medium follow the patterns of  $V_{PZ} < V_{P(45^\circ)} < V_{PX}{=}V_{PY}$ ,  $V_{SVZ}{=}V_{SHZ} = V_{SVX} = V_{SVY} < V_{SHX} = V_{SHY}$ . These patterns are largely repeated with V<sub>PX</sub> equal to V<sub>PY</sub> to within experimental uncertainty in nearly all cases and both substantially exceeding VPZ (Fig. 8a). Similarly, V<sub>SHX</sub>=V<sub>SHY</sub> and V<sub>SVX</sub>=V<sub>SVY</sub> as expected and these are significantly greater than the other measured  $V_S$ . The  $V_{SHZ}$  are usually close to  $V_{SVZ}$  but these can deviate from  $V_{SVX}$  and  $V_{SVY}$ (Fig. 8b). Taken together, these suggest that the material is close to TI, but it is unknown whether the small deviations are due to heterogeneity or to the sample being weakly orthorhombic. Although there are outliers that are likely due to sample heterogeneity, the VP trend tends to be lower with increasing organic content decreasing from 4045 to 3562 m/s in the bedding parallel directions (X, Y) and from 3272 to 2900 m/s in the vertical direction (Z), and linear fitting plots to the scatter data of P-wave velocities and kerogen content indicate that  $V_{PZ}$  (with gradient of -27.2) is more sensitive than  $V_{PX}$  and  $V_{PY}$  (with gradient of -26.1) to the increasing weight percentage of kerogen content. This can be reasonable explained that the increasing components of kerogen may induce similar reduction for the velocities in both directions due to the ductility characteristics of kerogen. However, the increasing content may also lead to enhancement of preferential alignments of kerogen (flow shaped kerogen in Fig. 5b) for the model under uniaxial stress during the construction of WCAS, which may moderate the declines of velocities paralleling to the bedding. V<sub>S</sub> for the samples is generally decreasing with the increase kerogen content. It is interesting to note that the response of V<sub>S</sub> behaved less sensitivity to the variations of kerogen content (with the gradient of approximate -500) than those of  $V_{P}$ .

Wave speeds by themselves, however, are controlled by a competition between the materials elasticity and density, and it is useful to also remove the effects of density and focus on the elastic parameters. The elastic stiffnesses can be obtained through Eqs. (2)-(6) and projected into crossplot with kerogen content (Fig. 9). All elastic stiffnesses except  $C_{13}$  are generally decreasing with the increasing kerogen content, and  $C_{11}$  and  $C_{33}$  decrease approximately 30 percent with kerogen content ranging from 1% to 15%, while  $C_{44}$  and  $C_{66}$  decrease approximately 11 percent during the increase of kerogen content. These results are indicative of greater



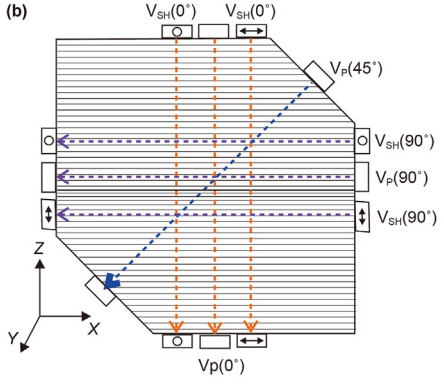


Fig. 7. (a) Experimental facility for ultrasonic pulse measurements; (b) diagram of the test method in the WCAS sample.

**Table 1**Basic parameters for the series of WCAS samples with different weight percentage of kerogen, where  $V_P(0^\circ)$  denotes the compressional wave velocity in the direction paralleling to the bedding,  $V_P(90^\circ)$  denotes the compressional wave velocity perpendicular to the bedding; x denotes no measured result.

| Model Num. | Kerogen<br>content,<br>% | V <sub>P</sub> (0°),  m/s | V <sub>P</sub> (45°), | V <sub>P</sub> (90°),  m/s | V <sub>SV</sub> (0°),<br>m/s | V <sub>SH</sub> (0°),  m/s | V <sub>SV</sub> (90°),<br>m/s | V <sub>SH</sub> (90°), | Porosity % | ε-δ   |
|------------|--------------------------|---------------------------|-----------------------|----------------------------|------------------------------|----------------------------|-------------------------------|------------------------|------------|-------|
|            |                          |                           |                       |                            |                              |                            |                               |                        |            |       |
| #2         | 3.36                     | 3910                      | x                     | 3303                       | 2086                         | 2304                       | 2145                          | 2081                   | 4.23       | x     |
| #3         | 4.96                     | 3726                      | 3500                  | 3233                       | 2016                         | 2219                       | 2064                          | 2064                   | 3.35       | 0.020 |
| #4         | 6.5                      | 3906                      | 3600                  | 3192                       | 2088                         | 2331                       | 2066                          | 2075                   | 2.86       | 0.069 |
| #5         | 8                        | 3665                      | 3378                  | 3057                       | 2089                         | 2378                       | 2001                          | 2001                   | 2.96       | 0.006 |
| #6         | 9.44                     | 3713                      | 3280                  | 3039                       | 2082                         | 2393                       | 1918                          | 1967                   | 3.09       | 0.208 |
| #7         | 10.16                    | 3773                      | 3513                  | 3053                       | 2033                         | 2257                       | 2019                          | 2019                   | 3.94       | 0.189 |
| #8         | 11.5                     | 3742                      | 3416                  | 3065                       | 2053                         | 2238                       | 2026                          | 2024                   | 5.12       | 0.008 |
| #9         | 12.2                     | 3724                      | 3460                  | 3064                       | 2009                         | 2234                       | 1984                          | 1991                   | 6.60       | 0.108 |
| #10        | 13.5                     | 3685                      | 3398                  | 3023                       | 2010                         | 2222                       | 1899                          | 1899                   | 4.69       | 0.058 |
| #11        | 14.8                     | 3562                      | X                     | 2900                       | 2045                         | 2243                       | 1976                          | 1909                   | 6.75       | x     |

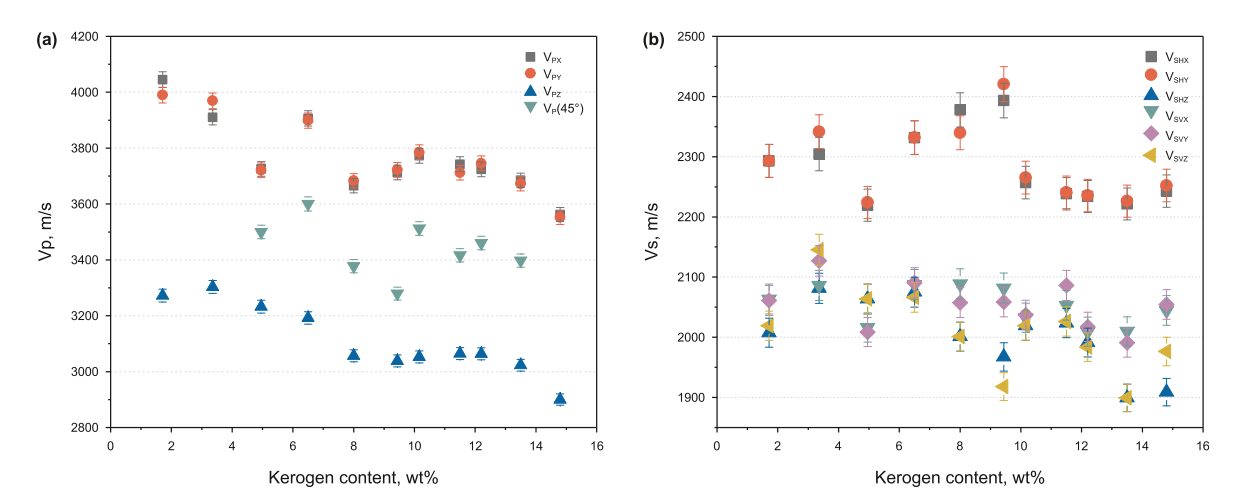


Fig. 8. (a) Compressional wave and (b) shear wave (V<sub>SH</sub> & V<sub>SV</sub>) ultrasonic velocities against kerogen content (wt %) in four directions of the samples.

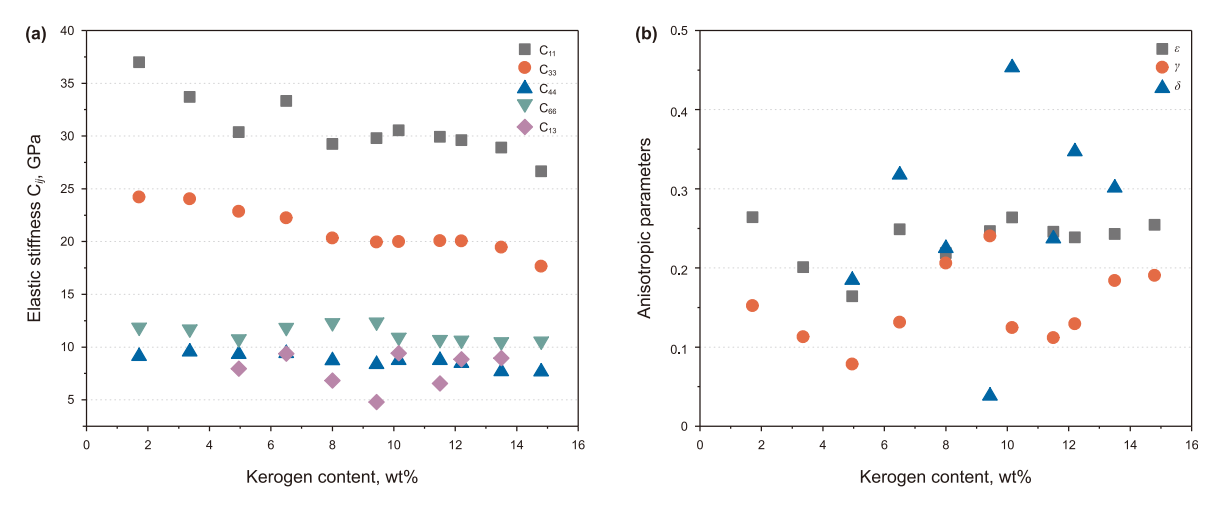


Fig. 9. (a) Elastic stiffness  $C_{ij}$  against the kerogen content, (b) plot of the kerogen content and P-wave & S-wave anisotropic parameters.

sensitivity to the variation of kerogen for P-wave type stiffnesses. It should be noted that  $C_{13}$  showed weak dependence on kerogen content. Fig. 9b shows the Thomsen parameters against kerogen content;  $\epsilon$  and  $\gamma$  have not systematically varied trend to the kerogen content; and  $\delta$  appears weak dependence to the kerogen content as well. It may due to the overall influence of different structural components within the kerogen. However, both the compressional

wave and shear wave anisotropy for the series of samples with different kerogen contents are greater than 10%, and the strongest anisotropy can reach 26% for  $\varepsilon$  and 24% for  $\gamma$ , which mean the series of WCAS samples exhibit strong anisotropy for both compressional and shear waves. Note that magnitude of  $\delta$  for all the WCAS with different kerogen contents are positive and the maximum value reaches 0.54. Additionally, anisotropic parameter  $\delta$  is generally

greater than the values of  $\varepsilon$  and  $\gamma$  for the WCAS with the same kerogen content (similar to Nadri et al., 2011).

With the measured five stiffnesses, dynamic Young's modulus and Poisson's ratios can be derived by using Eqs. (10)-(14). As shown in Fig. 10a,  $E_1$  substantially exceeds  $E_3$  for all the samples with the same kerogen content, which is in consistence with the published observations in natural shale (Ong et al., 2016), and they are generally decreasing with the increasing kerogen content. Linear fitting curves to the scatter data of dynamic Young's modulus  $(E_1 \& E_3)$  and kerogen content indicate  $E_3$  (with gradient of -3.26) are more sensitive to the variation of kerogen content than those of  $E_1$  (with gradient of -2.68). The corresponding dynamic Poisson's ratios calculated from Eqs. (12)-(14) are given in Fig. 10b, for the series of samples in this study,  $v_{13}$  tends to be greater with the increase of kerogen content, while  $v_{12}$  and  $v_{31}$  are generally independent of the kerogen content. Note that  $v_{13}$  are generally greater than  $v_{12}$  and  $v_{31}$  for the WCAS with the same kerogen content, and the differences in between seem tend to be greater with the increasing weight percentage of kerogen content. Another interesting observation should be noted that  $v_{12}$  is not always equal to  $v_{31}$ , and this phenomenon reveals that the dynamic E and  $\nu$  of WCAS exhibit anisotropic characterizations.

The dynamic anisotropic mechanical parameters (DAMP) can be obtained through Eqs. (15)-(19) and projected into crossplot with kerogen content (Fig. 11a), anisotropic parameters for Young's modulus ( $\Delta E$ ), Poisson's ratio ( $\Delta v$ ) and Brittleness ( $\Delta B$ ) are generally larger than 0.2 and exhibit strong anisotropy for the WCAS with different kerogen contents.  $\Delta E$  and  $\Delta B$  tend to decrease with the reducing kerogen content, and  $\Delta B$  is more sensitive to the variation of kerogen content with relative drop as large as 54% with the decreasing kerogen content in the range from 14.8% to 1.71%. The relationship between  $\Delta v$  and kerogen content is complicated, which makes interpretation difficult. Fig. 11b shows the V<sub>P</sub>/V<sub>SH</sub> ratio against variation of kerogen content. In relatively low kerogen content (less than 10%), the V<sub>P</sub>/V<sub>SH</sub> ratios are linearly decreasing with the increase of kerogen content. V<sub>P</sub>/V<sub>SH</sub> ratio in the horizontal direction linearly decrease from 1.733 to 1.538 with the kerogen content increase from 1.71% to 9.44%, while in the vertical direction the decrease trend is moderate, and one possible explanation for the low V<sub>P</sub>/V<sub>S</sub> ratio in organic-rich shales might be the microcracks provided by organic matters. Due to the previous laboratory study reported by Ding et al. (2019), the dry randomly oriented cracks caused low V<sub>P</sub>/V<sub>S</sub> ratio. The organic matter weight could increase

the microcrack development in shale, and cause the lower  $V_P/V_S$  ratio in shales with high kerogen content. In the range of high kerogen content (more than 10%), there is no evident correlation between the  $V_P/V_{SH}$  ratio and kerogen content. However, one interesting phenomenon is that WCAS with high kerogen content characterized by the corresponding  $V_P/V_{SH}$  typically less than 1.75.

## 5. Discussions

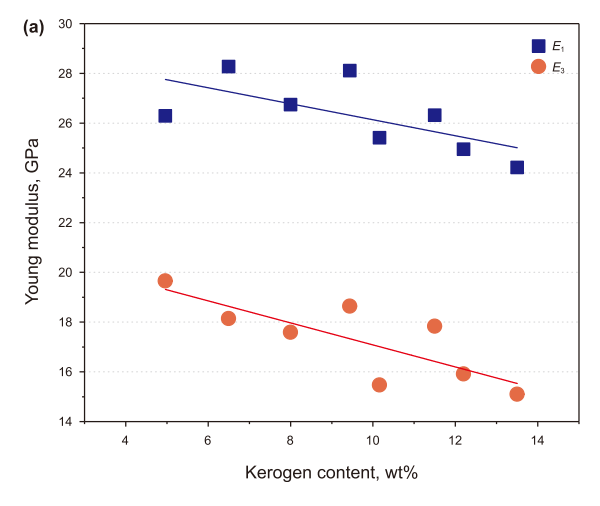
## 5.1. Anisotropic dynamic mechanical properties

In real field situations,  $V_P$  and  $V_S$  data can usually only be obtained from acoustic logging. For an elastically isotropic formation the ratio  $V_P/V_S$  and the apparent dynamic Poisson's ratio  $\nu$  & Young's modulus E:

$$\nu_{\text{Apparent}} = \frac{1}{2} \frac{\left(\frac{V_p}{V_s}\right)^2 - 2}{\left(\frac{V_p}{V_s}\right)^2 - 1}$$
 (20)

$$E_{\text{Apparent}} = \rho V_{\text{S}}^2 \frac{3\left(\frac{V_{\text{P}}}{V_{\text{S}}}\right)^2 - 4}{\left(\frac{V_{\text{P}}}{V_{\text{S}}}\right)^2 - 1}$$
(21)

which are both used to provide qualitative indication of the materials brittleness or of mineralogic content. In the usual situation, a vertical borehole crosses a geological formation with horizontal bedding and hence one would obtain (with reference to Fig. 7b) measures of  $V_{PZ}$  and  $V_{SHZ}$  (= $V_{SVZ}$ ) with the associated ratio V<sub>PZ</sub>/V<sub>SHZ</sub>. At the other extreme with a horizontal borehole, one might measure  $V_{PX}$  (= $V_{PY}$ ) and the fastest shear wave  $V_{SHX}$  (= $V_{SHY}$ ) allowing calculation of ratio (V<sub>PX</sub>/V<sub>SHX</sub>). These ratios can provide apparent values of E and  $\nu$  if substituted into Eqs. (20) and (21). Apparent dynamic Poisson's ratio  $\nu$  in the bedding paralleling and perpendicular orientations are also projected in Fig. 10b as shown in Fig. 12a, and the plots show that  $v_X$  and  $v_Z$  have good agreement with the true dynamic Poisson's ratio  $v_{31}$  and  $v_{12}$  for the sample with same kerogen. True versus apparent relation for dynamic Young's modulus (E) in horizontal and vertical directions are plotted in Fig. 12b, different colors represent different kerogen contents. The error of using these isotropic equations rather than



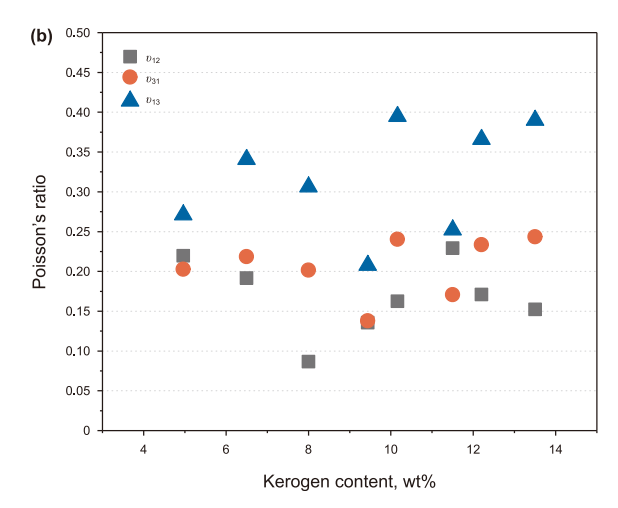


**Fig. 10.** (a) Dynamic E and (b)  $\nu$  as function of the weight percentage of kerogen content from 1% to 15%.  $E_1$  and  $E_3$  are dynamic Young's modulus along and normal to the bedding plane, respectively. Blue and red line denote the linear regression curves for  $E_1$  and  $E_3$  at different kerogen contents.

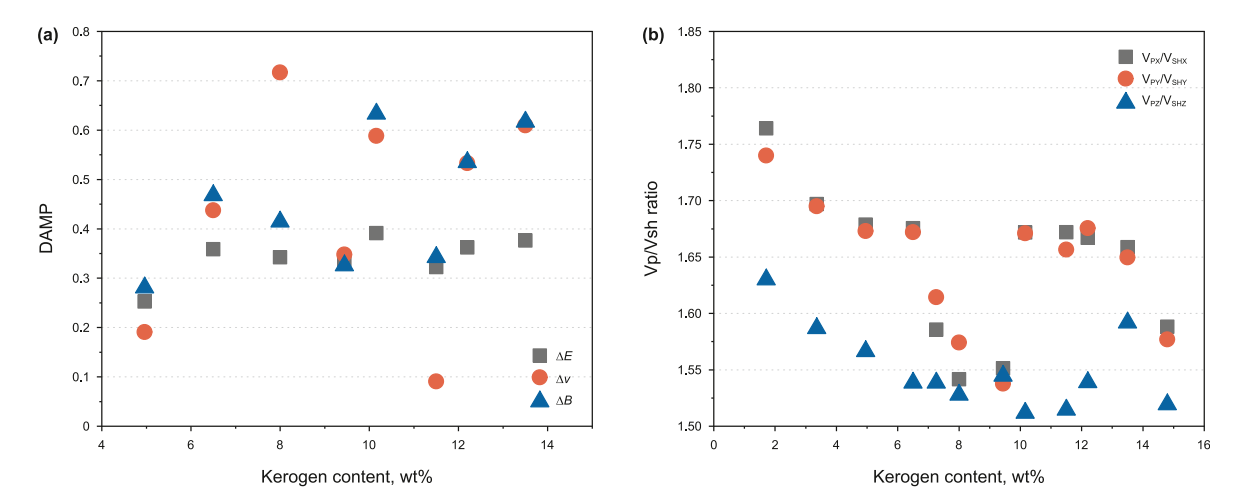


**Fig. 11.** (a) Crossplot of dynamic anisotropic mechanical parameters (DAMP) and kerogen content,  $\Delta E$  and  $\Delta \nu$  denote Young's modulus anisotropic parameter and Poisson's ratio anisotropic parameter,  $\Delta B$  denotes the Brittleness anisotropic parameter. (b) Compilation of the measured V<sub>P</sub>/V<sub>SH</sub> ratio in three directions of the cubic WCAS samples and weight percentage of kerogen content in WCAS samples.

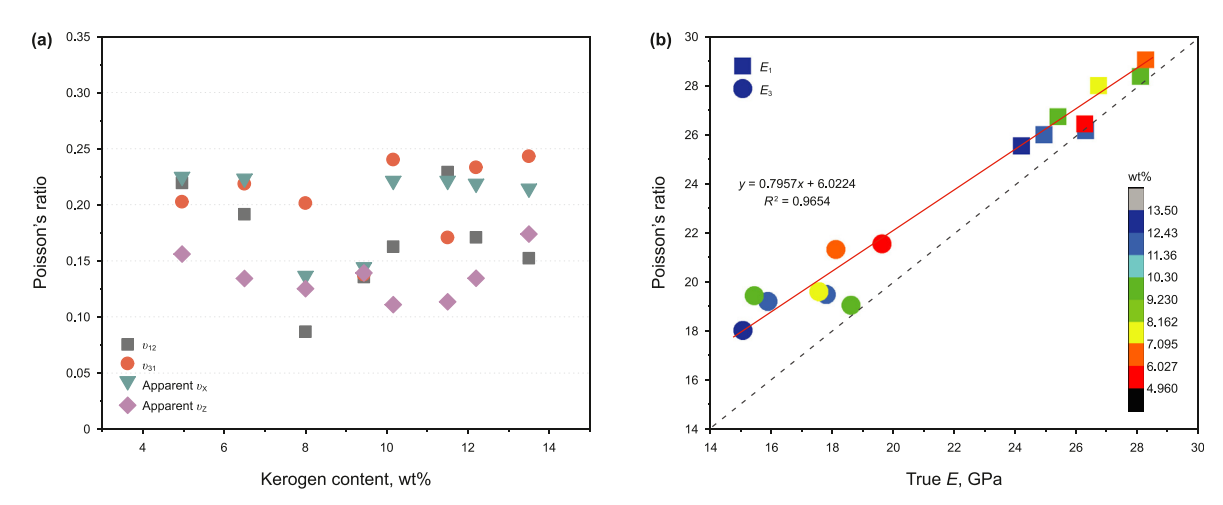


**Fig. 12.** (a) Apparent and true dynamic Poisson's ratio  $\nu$  in the bedding paralleling and perpendicular orientations as function of kerogen content. (b) Apparent versus true relation for dynamic Young's modulus, different colors represent different kerogen contents. The black dash denotes one-to-one crossplot, the red solid line represents the linear regression curve to the projected data.

the complete anisotropic equations was small, and the correlation can be described as linear regression curve with Pearson coefficient of 0.96. Additionally, the true and apparent E in horizontal directions are more close to one-to-one correspondence (black dash line) than that in vertical direction. In this sense, although it must be stressed that these values are strictly incorrect as one cannot determine a Poisson's ratio and Young's modulus without information of wave speed measurements away from the principal symmetry axes in an anisotropic TI medium, the apparent dynamic mechanical properties ( $\nu$  and E) may effectively substitute the true ones to solve the engineering problem in certain circumstance regardless of the variation of kerogen content.

## 5.2. Estimation of kerogen content from $V_P/V_S$ ratios

Despite the significant influence on the physical properties of shale, however, the effects of kerogen contents on the dynamic properties are inherently complex and it is difficult to quantitative discriminate on a real shale sample, which makes the topic still far from being elucidated. However, with the success of the constructed WCAS, the kerogen content can be accurate quantified,

then to investigate its effect on the physical properties of framework separately.

Based on the measured observations on the WCAS, at relatively low kerogen content (0-10%), V<sub>P</sub>/V<sub>S</sub> ratio and the weight percentage of kerogen have linearly negative correlation. It demonstrated that the magnitude of V<sub>P</sub>/V<sub>S</sub> ratio may be a sensitive parameter to predict the kerogen content in both the directions of parallel and perpendicular to the bedding. This correlation has implications to derive empirical formulation for the use of advance hydrocarbon prediction during the field exploration. Since it is relatively easy to obtain corresponding V<sub>P</sub>/V<sub>S</sub> ratio for a region of interest from modern sonic logs. Furthermore, compared to the density or velocities, V<sub>P</sub>/V<sub>S</sub> ratio tends to be a more unique parameter, as is known, it is a very significant factor for differentiating lithology. At relatively high kerogen content (weight percentage more than 10%), the magnitude of  $V_P/V_S$  ratio is generally less than 1.75, which would be a significant and typical indicator for organic-rich shale.

To further verify the relationship between the  $V_P/V_S$  ratio and kerogen content, we collected multiple published data sets from literature (Vernik and Liu, 1997) in shale cores. Fig. 13a and b show

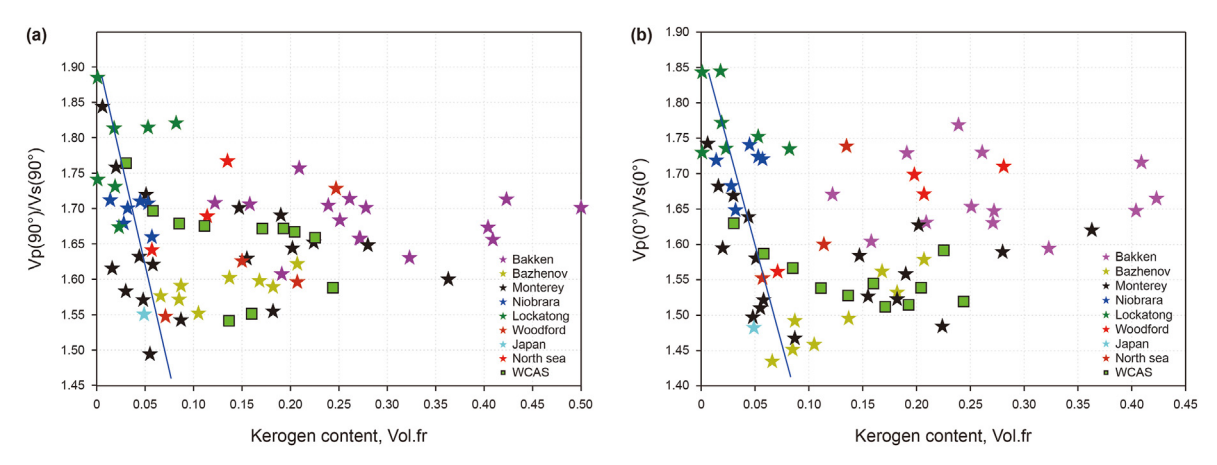


Fig. 13. Compilation of the  $V_P/V_S$  ratio and volume fraction of kerogen in (a) horizontal and (b) vertical direction to the bedding in the natural shale and WCAS. Green squares denote the corresponding data of WCAS. Blue line represents the trend line for the data in the range of 0–10% kerogen content.

the crossplot of V<sub>P</sub>/V<sub>S</sub> ratio in the bedding-normal & beddingparallel direction and volume fraction of kerogen. V<sub>P</sub>/V<sub>S</sub> ratio sharply decreases with increase of kerogen volume fraction in the range of 0-10% (relatively low percentage) independent of the regions and wave-propagation directions. In the range of relatively high volumes proportion of kerogen (more than 10%), the correlation between V<sub>P</sub>/V<sub>S</sub> ratio and kerogen content tend to be weak. Nevertheless, we can find a similar interesting phenomenon from the plot as shown in Fig. 11, and the crossplot exhibits the specialty of the high organic-rich shales characterized by the V<sub>P</sub>/V<sub>S</sub> that is less than 1.75, which indicated that the V<sub>P</sub>/V<sub>S</sub> ratio low than 1.75 is a good indicator for organic-rich shale. Both in bedding parallel and perpendicular directions, they show the similar phenomena as the experimental measured data did. Actually, according to the template of V<sub>P</sub> and V<sub>S</sub> for dipole sonic data that are obtained in wells from Bakken, Woodford and Bossier shales, Vernik and Milovac (2011) concluded that magnitude of V<sub>P</sub>/V<sub>S</sub> in shale located in relatively narrow range from 1.6 to 1.7, independent of the directions, which is also consistent with our observations. Therefore, we can further conclude that kerogen content may be the fatal and major factors affected the variation of V<sub>P</sub>/V<sub>S</sub> ratio. For further comparison, we computed the volume fraction from weight percentage of the kerogen with the measured data based on the transition equation by Vernik and Milovac (2011), and the density for the kerogen analogs is 1.5 g/cm<sup>3</sup>, then we project the data into the plots of natural shale, as shown in Fig. 13, green squares denote the corresponding data of WCAS. Similar observations from the above plots can be obtained, it is interesting to be noted that linear decreasing trend can be observed at low content (<10%) for both in the range of weight percentage and the volume fraction of kerogen content. It should be noted that the cross plot of  $V_P/V_S$  and kerogen content of natural cores are generated from the multiple wells, and the corresponding trendline behaves great consistency to those of WCAS. However, such observation is not always true for the nature shale since V<sub>P</sub>/V<sub>S</sub> could be affected by various factors (mineral components, micro-structure, kerogen type etc.). More quantitative measurements on natural shales should be carried on to make further verification.

## 6. Conclusions

Hot-pressing technique, which considers both diagenetic pressure and temperature, was utilized to produce a series of 11 well-controlled artificial organic shale (WCAS) blocks with varying weight percentages of kerogen content ranging from approximately 1%—15%. Quantitative correlations are bridged between

kerogen content and anisotropic dynamic properties based on WCAS samples. V<sub>P</sub> and V<sub>S</sub> velocities measured in bedding parallel and perpendicular directions are consistent with the material having transversely isotropic symmetry. The P-wave velocities in the direction perpendicular to the bedding plane display higher sensitivity to changes in kerogen content compared to those in the bedding-parallel directions. Anisotropic parameters  $\varepsilon$  and  $\gamma$  have not systematically varied trend to the kerogen content. Comparisons of the observation of apparent dynamic mechanical parameters (E and  $\nu$ ) and true ones, the linear relationship with organic compositions may hold great value towards the interpretation of well logs through consistent formations. Anisotropic mechanical parameters ( $\Delta E$  and  $\Delta B$ ) tend to decrease with the reducing kerogen content, and  $\Delta B$  is more sensitive to their variation. The kerogen contents are linearly controlling V<sub>P</sub>/V<sub>S</sub> ratio low kerogen content (typically less than 10%). Comparison of such ratios from a compilation of values taken from the literature for a variety of organic rich shales globally further proves the relation, which may help identify a "sweet-pot" in the subsurface and quantify distribution, thickness, and richness for shale reservoirs.

## **Declaration of competing interest**

The authors declare that they have no known competing financial interests or personal relationships that could have appeared to influence the work reported in this paper.

## Acknowledgements

This research is supported by the National Natural Science Foundation of China (42004112, 42274175, 42030812, 41974160), Natural Science Foundation of Sichuan Province (2023NSFSC0764). The data or code relating to this work are available by contacting the corresponding author.

## References

Allan, A.M., Kanitpanyacharoen, W., Vanorio, T., 2015. A multiscale methodology for the analysis of velocity anisotropy in organic-rich shale. Geophysics 80 (4), C73—C88. https://doi.org/10.1190/geo2014-0192.1.

Alsinan, S., 2017. Effect of artificially induced maturation on the elastic properties of kerogen. SEG Technical Program Expanded Abstracts, pp. 3647–3652. https:// doi.org/10.1190/segam2017-17257552.1.

Altowairqi, Y., Rezaee, R., Evans, B., et al., 2015. Shale elastic property relationships as a function of total organic carbon content using synthetic samples. J. Petrol. Sci. Eng. 133, 392–400. https://doi.org/10.1016/j.petrol.2015.06.028.

Baird, A.F., Kendall, J.M., Fisher, Q.J., et al., 2017. The role of texture, cracks, and fractures in highly anisotropic shales. J. Geophys. Res. Solid Earth 122 (12),

- 10341-10351. https://doi.org/10.1002/2017JB014710.
- Banik, N.C., 1984. Velocity anisotropy of shales and depth estimation in the North Sea basin. Geophysics 49 (9), 1411–1419. https://doi.org/10.1071/EG984189.
- Beloborodov, R., Pervukhina, M., Lebedev, M., 2017. Compaction trends of full stiffness tensor and fluid permeability in artificial shales. Geophys. J. Int. 212 (3), 1687-1693. https://doi.org/10.1093/gji/ggx510.
- Bohacs, K.M., Grabowahi, G.J., Carroll, A.R., et al., 2005. Production, destruction, and dilution-The many paths to Source-Rock development, Deposition Org. Carbon-Rich Sediments: Models Mech. SEPM Special Publications 82, 61–102. https://doi.org/10.2110/pec.05.82.0061.
- Bowker, K.A., 2002, Recent Developments of the Barnett Shale Play, Fort Worth Basin, In: Innovative Gas Exploration Concepts Symposium.
- Dewhurst, D.N., Siggins, A.F., 2006. Impact of fabric, microcracks and stress field on shale anisotropy. Geophys. J. Int. 165 (1), 135-148. https://doi.org/10.1111/ i.1365-246X.2006.02834.x.
- Ding, P., Wang, D., Di, G., et al., 2019. Investigation of the effects of fracture orientation and saturation on the V<sub>P</sub>/V<sub>S</sub> ratio and their implications. Rock Mech. Rock Eng. 52 (9), 3293-3304. https://doi.org/10.1007/s00603-019-01770-3
- Ding, P., Wang, D., Gong, F., et al., 2020b. Laboratory observation of velocity anisotropy affected by clays and microcracks in artificial clay-rich shale samples. J. Petrol. Sci. Eng. 191, 107156. https://doi.org/10.1016/j.petrol.2020.107156. Ding, P., Wang, D., Li, X.Y., 2020a. An experimental study on scale-dependent ve-
- locity and anisotropy in fractured media based on artificial rocks with controlled fracture geometries. Rock Mech. Rock Eng. 53 (7), 3149-3159. https://doi.org/10.1007/s00603-020-02095-2.
- Ding, P.B., Gong, F., Zhang, F., et al., 2021. A physical model study of shale seismic responses and anisotropic inversion. Petrol. Sci. 18 (4), 1059-1068. https:// doi.org/10.1016/i.petsci.2021.01.001.
- Hornby, E.B., 1998. Experimental laboratory determination of the dynamic elastic properties of wet, drained shales. J. Geophys. Res. 103 (B12), 945-964. https:// doi.org/10.1029/97IB02380.
- Jiang, Y., Dong, D., Qi, L., et al., 2010. Basic features and evaluation of gas reservoir. Nat. Gas. Ind. 30 (10), 7–12. https://doi.org/10.1016/S1876-3804(11)60008-6. (in Chinese).
- Johnston, J.E., Christensen, N.I., 1995. Seismic anisotropy of shales. J. Geophys. Res. Solid Earth 100, 5991-6003. https://doi.org/10.1029/95JB00031.
- Jones, L.E.A., Wang, H.F., 1981. Ultrasonic velocities in Cretaceous shales from the Williston basin. Geophysics 46 (3), 288-297. https://doi.org/10.1190/1.1441199.
- Kaarsberg, E.A., 1959. Introductory studies of natural and artificial argillaceous aggregates by sound-propagation and X-ray diffraction methods. J. Geol. 67, 447-472. https://doi.org/10.1086/626597
- Kanitpanyacharoen, W., Wenk, H., Kets, F., 2011. Texture and anisotropy analysis of Qusaiba shales. Geophys. Prospect. 59, 536-556. https://doi.org/10.1111/ i.1365-2478.2010.00942.x.
- Khatibi, S., Ostadhassan, M., Tuschel, D., et al., 2017. Raman spectroscopy to study thermal maturity and elastic modulus of kerogen. Int. J. Coal Geol. 185, 103-118. https://doi.org/10.1016/j.coal.2017.11.008.
- Li, C., Xie, H., Wang, J., 2020. Anisotropic characteristics of crack initiation and crack damage thresholds for shale. Int. J. Rock Mech. Min. Sci. 126, 104178. https:// doi.org/10.1016/j.ijrmms.2019.104178
- Løseth, H., Wensaas, L., Gading, M., et al., 2011. Can hydrocarbon source rocks be identified on seismic data? Geology 39 (12), 1167-1170. https://doi.org/10.1130/
- Luan, X.Y., Wei, J.X., Di, B.R., et al., 2014. Laboratory measurements of brittleness anisotropy in synthetic shale with different cementation. SEG Tech. Progr. Expand. Abstr. 3005-3009. https://doi.org/10.1190/segam2014-0432.1
- Luan, X., Di, B., Wei, J., 2016. Creation of synthetic samples for physical modelling of natural shale. Geophys. Prospect. 64 (4), 898-914. https://doi.org/10.1111/1365-
- Mah, M., Schmitt, D.R., 2001. Experimental determination of the elastic coefficients of an orthorhombic material. Geophysics 17 (66), 410-412. https://doi.org/
- Mavko, G., Mukerji, T., Dvorkin, J., 2009. The Rock Physics Handbook: Tools for Seismic Analysis of Porous Media. Cambridge University Press. https://doi.org/ 10.1017/CBO9780511626753
- Montgomery, S.L., Jarvie, D.M., Bowker, K.A., et al., 2005. Missippian barnett shale, fort worth basin, north-central Texas: gas-shale play with mulirillion cubic foot potential. AAPG (Am. Assoc. Pet. Geol.) Bull. 89 (2), 155-175. https://doi.org/
- Nadri, D., Bona, A., Brajanovski, M., 2011. Estimation of stressdependent anisotropy

- from P-wave measurements on a spherical sample. Geophysics 76 (3), WA91-WA100. https://doi.org/10.1190/1.3552703.
- Ong, O.N., Schmitt, D.R., Kofman, R.S., et al., 2016. Static and dynamic pressure sensitivity anisotropy of a calcareous shale. Geophys. Prospect. 64 (4), 875–897. https://doi.org/10.1111/1365-2478.12403.
- Passey, Q.R., Bohacs, K., Esch, W.L., et al., 2010. From oil-prone source rock to gas-producing shale reservoir-geologic and petrophysical characterization of unconventional shale gas reservoirs. Int. Oil and Gas Conf. Exhib. China. https:// doi.org/10.2118/131350-MS.
- Prasad, M., Sadler, T., Batzle, M.L., 2011. Maturity and impedance analysis of organicrich shales. SPE Reservoir Eval. Eng. 14, 533-543. https://doi.org/10.2118/ 123531-PA
- Rickman, R., Mullen, M., Petre, E., et al., 2008. Practical Use of Shale Petrophysics for Stimulation Design Optimization: All Shale Plays Are Not Clones of the Barnett Shale. Society of Petroleum Engineers, Richardson, TX, USA. https://doi.org/ 10.2118/115258-MS
- Sarout, J., Molez, L., Gueguen, Y., et al., 2007. Shale dynamic properties and anisotropy under triaxial loading: experimental and theoretical investigations. Phys. Chem. Earth 32, 896–906. https://doi.org/10.1016/j.pce.2006.01.007.
- Sayers, C.M., Boer, L.D., 2019. The impact of different clay minerals on the anisotropy of clay matrix in shale. Geophys. Prospect. 67 (9), 2298-2318. https://doi.org/ 10 1111/1365-2478 12829
- Sayers, C.M., 2005. Seismic anisotropy of shales. Geophys. Prospect. 53 (5), 667-676. https://doi.org/10.1111/j.1365-2478.2005.00495.x.
- Sone, H., Zoback, M.D., 2013. Mechanical properties of shale-gas reservoir rocks Part 1: static and dynamic elastic properties and anisotropy. Geophysics 78 (5), D378-D389. https://doi.org/10.1190/geo2013-0050.1.
- Sonnenberg, S.A., Pramudito, A., 2009. Petroleum geology of the giant elm coulee field, williston basin. AAPG Bull. 93, 1127-1153. https://doi.org/10.1306/ 05280909006
- Thomsen, L., 1986. Weak elastic anisotropy. Geophysics 51 (10), 1954–1966. https:// doi.org/10.1144/SP284.14.
- Tissot, W.D.H., Bernard, P., 1984. Petroleum Formation and Occurrence. Springer-
- Verlag, pp. 643-644. https://doi.org/10.1007/978-3-642-87813-8. Vernik, L., Milovac, J., 2011. Rock physics of organic shales. Lead. Edge 30 (3), 318-323. https://doi.org/10.1190/1.3567263.
- Vernik, L., Liu, X., 1997. Velocity anisotropy in shales: a petrophysical study.
- Geophysics 62 (2), 521–532. https://doi.org/10.1190/1.1444162. Wenk, H.R., Lonardelli, I., Franz, H., et al., 2007. Preferred orientation and elastic anisotropy of illite-rich shale. Geophysics 72 (2), E69-E75. https://doi.org/ 10.1190/1.2432263
- Xie, J., Di, B., Wei, J., et al., 2016. Feasibility analysis of a kerogen analogue used in the construction of artificial organic-rich shale samples. In: 78th EAGE Conference and Exhibition. https://doi.org/10.3997/2214-4609.201601572
- Xie, J., Di, B., Wei, J., et al., 2015. Feasibility of theoretical formulas on the anisotropy of shale based on laboratory measurement and error analysis. J. Geophys. Eng. 12 (3), 253-261. https://doi.org/10.1088/1742-2132/12/2/253.
- Xie, J., Cao, J., Schmitt, D.R., et al., 2019. Effects of kerogen content on elastic properties-based on artificial organic-rich shale (AORS). J. Geophys. Res. Solid Earth 124 (12), 12660-12678. https://doi.org/10.1029/2019JB017595
- Xie, J., Di, B., Schmitt, D.R., et al., 2018. Estimation of  $\delta$  and  $C_{13}$  of organic-rich shale from laser ultrasonic technique measurement. Geophysics 83 (4), C137-C152. https://doi.org/10.1190/geo2017-0512.1.
- Yin, H., 1992. Acoustic Velocity and Attenuation of Rocks: Isotropy, Intrinsic Anisotropy, and Stress Induced Anisotropy. Ph.D. thesis, Department of Geophysics, School of Earth Sciences, Stanford Univ.
- Yu, H., Rezaee, R., Wang, Z., et al., 2017. A new method for TOC estimation in tight shale gas reservoirs. Int. J. Coal Geol. 179, 269-277. https://doi.org/10.1016/ j.coal.2017.06.011.
- Zargari, S., Prasad, M., Mba, K.C., et al., 2013. Organic maturity, elastic properties, and textural characteristics of self-resourcing reservoirs. Geophysics 78 (4), D223-D235. https://doi.org/10.1190/geo2012-0431.1.
- Zhao, L., Qin, X., Zhang, J., et al., 2018. An effective reservoir parameter for seismic characterization of organic shale reservoir. Surv. Geophys. 39 (3), 509-541. https://doi.org/10.1007/s10712-017-9456-9.
- Zhu, Y., Xu, S., Liu, E., et al., 2013. Predicting anisotropic source rock properties from well data: U.S. Patent Appl. 13/521, 948.
- Zhu, Y., et al., 2011. Understanding geophysical responses of shale gas plays. Lead. Edge 30 (3), 332-338. https://doi.org/10.1190/1.3567265.